Mixed mode ductile fracture of an anisotropic 2024 Al-Cu alloy

Yazid Madi, Jacques Besson, Franck Tankoua, Jianqiang Chen, Naman Recho

Mixed-mode ductile fracture of an anisotropic 2024 Al-Cu Alloy

Yazid MADI[1,2], Jacques BESSON[2], Franck TANKOUA[1,2], Jianqiang CHEN[2], Naman RECHO[1]

[1]Ermess EPF-Ecole d'Ingénieurs
3 bis rue Lakanal 92330 Sceaux
France
yazid.madi@epf.fr

[2]Centre des Matériaux
Mines ParisTech, UMR CNRS 7633
BP 87, 91003 Evry Cedex, France
jacques.besson@ensmp.fr

Abstract: Assessment of structural integrity of structures often requires investigating the combination of tensile (Mode I) and shearing (Mode II) or tearing (Mode III) loadings. The purpose of this study is to shed some light on the ductile mixed-mode fracture process and its underlying mechanics. Ductile rupture of a 2024 Al Alloy thin sheet is investigated under mixed-mode loading. Mechanical tests are carried out on smooth and specific mixed-mode Arcan specimens. Test data on smooth samples are used to identify the parameters of constitutive equations describing plastic anisotropy. Digital image correlation (DIC) technique is used to measure the local displacement in the vicinity of the V-notch. Using these measurements an analysis of the effect of mixed-mode loading on ductile crack initiation is performed. Failure mechanisms are investigated using scanning electron microscope (SEM). Results are finally interpreted and modeled using a simple local approach based on the Rice and Tracey criterion.

Key–Words: Mixed mode, ductile rupture, Rice and Tracey, Digital Image Correlation, δ_5, 2024 Al-Cu.

1 Introduction

Assessment of structural integrity of structures often requires investigating the combination of tensile (Mode I) and shearing (Mode II) or tearing (Mode III) loadings. Numerous investigations have dealt with brittle material or fatigue loading (see review in [1]). The case of ductile fracture has been less studied in particular in cases of extended plasticity (Large Scale Yielding: LSY). This is the case of ductile tearing of thin metal sheets [2] or of welded structures (see e.g. [3]). Even for pure mode I macroscopic loading, local mixed-mode can be observed as in the case of slant fracture (I+III modes) as illustrated in Fig. 1 [4]. Microstructural observations indicated that there were two failure mechanisms: void growth and coalescence (classical ductile fracture: regions with a high stress triaxiality[1]), and shear localization and decohesion (ductile shear fracture: regions with a low stress triaxiality). The reason why slant fracture occurs is still not well understood. Several experimental studies (e.g. [5, 6]) introduced an external shear loading (mixed-mode loading) to modify the local state of stress triaxiality (or plastic constraint) to promote one mechanism over another. [7] showed that these mechanisms can be related to the local Mode I and Mode II components of the J-Integral (Global Approach of Fracture). These results were limited to the

Small Scale Yielding (SSY) conditions where plasticity is supposed to be confined around the crack or the notch. For the case of Large Scale Yielding (LSY) conditions, the present topic of interest, another technique may be used to achieve the objectives: the local approach of fracture [8, 9]. This approach is able to deal with the situations where no preexisting crack is present and to predict both the location of crack initiation and crack path. Within this framework, damage and rupture can be represented on a surface (cohesive zone model) or in the volume (continuum damage mechanics).

The purpose of the this study is to shed some light on the ductile mixed-mode fracture process and its underlying mechanics. Ductile rupture of a 2024 Al Alloy thin sheet is investigated under mixed-mode loading. The paper is organized as follows. First mechanical test are carried out on smooth and specific mixed-mode Arcan specimens, Fig. 2. Test data on smooth samples are used to identify the parameters of constitutive equations describing plastic anisotropy. Digital image correlation (DIC) technique is used to measure the local displacement in the vicinity of the V-notch. Using these measurements an analysis of the effect of mixed-mode loading on ductile crack initiation is performed. Failure mechanisms are investigated using scanning electron microscope (SEM). Results are finally interpreted and modeled using a simple local approach type model for ductile failure.

---

[1]The stress triaxiality ratio is defined as: $\tau = \frac{\sigma_m}{\sigma_{eq}}$ where σ_m is the mean stress and σ_{eq} the von Mises equivalent stress.
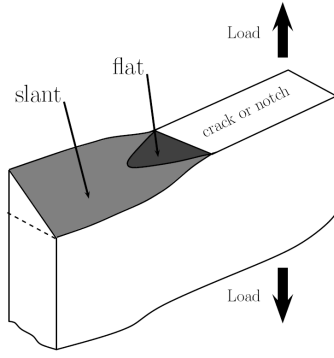
Figure 1: Flat to slant transition in metal sheets.

2 Materials

The study was performed on 2024 aluminum alloy sheets with a nominal thickness of 1.73 mm. This material, studied in [10, 11, 12] and supplied by Alcan Centre de Recherches de Voreppe (CRV), is a high purity alloy improved for high damage tolerance. Table 1 gives its chemical composition. The grade was solution heat-treated, quenched and naturally aged to a substantially stable condition (T4). To avoid corrosion the sheets are covered with a thin cladding (less than 80 μm) of 1050 aluminum on both faces. In the following, the rolling direction is referred to as L, the long transverse direction as T and the short transverse direction (thickness) as S. All specimens used in this work were machined from a single plate of the 2024 material (slightly different from that studied by Bron *et al.*).

Cu	Mn	Mg	Si	Fe	Al
3.8-4.9	0.3-0.9	1.2-1.8	0.04	0.07	remainder

Table 1: Chemical composition of 2024 material alloy (wt %), [11].

3 Experimental setup and testing conditions

In order to characterize the mechanical behavior, two specimen types were used (Fig. 2). The ST_{12} sample is a conventional smooth flat tensile specimen used to determine the elastic-plastic behavior. Smooth tensile specimens were tested using two displacement gages so that both longitudinal and transverse strain were recorded.

Arcan samples were used to study the fracture behavior for three different loading conditions character-

ized by the angle β between the machined notch and the loading direction. Values for β were: $\beta = 30°$, $60°$ and $90°$. $90°$ corresponds to pure macroscopic mode I (see Fig. 2). Two configurations were compared with the notch machined either along the L direction or the T direction ; they will be referred to as L_N and T_N in the following. All tests are carried out at room temperature on a 50 kN servo-hydraulic testing machine under displacement control with a displacement rate equal to $0.2mm/min$. In this study a monoblock Arcan specimen was designed whereas smaller samples attached to a setup allowing to vary the loading direction are often used in the literature (see e.g. [6]). This specimen allows to better control and monitor loading on the specimen so that comparisons can more easily be made with finite element simulations.

Digital Image correlation (DIC) technique was used to follow the deformation of Arcan specimens by tracking the displacement of predefined marks in the vicinity of the V-notch. Two marks are located at ± 2.5 mm from the notch tip to measure the δ_5 displacement as proposed in [13]. Two other marks are used to measure the Crack Mouth Opening Displacements (CMOD) at 7 mm from the crack tip as done in [14]. The position of the different marks is sketched in fig. 3. In both cases, the relative displacement of both marks can be decomposed into normal and parallel components with respect to the notch direction.

The technique was applied using a mobile equipment: combination of a SPOT Insight Digital Camera, a computer and a correlation software. The main features of the Digital Camera are: a CCD resolution of 2048 x 2048 pixels, a sensor pixel size of 7.4 μm square pixels and 14 bits for intensity resolution. Its accuracy is closely related to several factors (such as the quality of the random speckle, lighting, CCD sensor, optical lens. . .). For the experiments the distance between the camera and the specimen is ≈ 340 mm and the typical magnification factors is 70 pixels/mm. It is also important to set-up a specific process to minimize all sources of errors related to DIC technique. Guidelines are proposed in recently published works [15, 16] to minimize and to correct these errors.

4 Fractography

As depicted in Fig. 1 fracture surface in Arcan test samples is always initiated at the middle of the notch where the fracture surface is flat along the notch direction. This region forms a small triangle. Outside this zone, slant fracture is observed. A closer examination of the fracture surfaces, shows void growth around the iron/copper particles. Void growth is more pronounced in the flat fracture region than in the slant
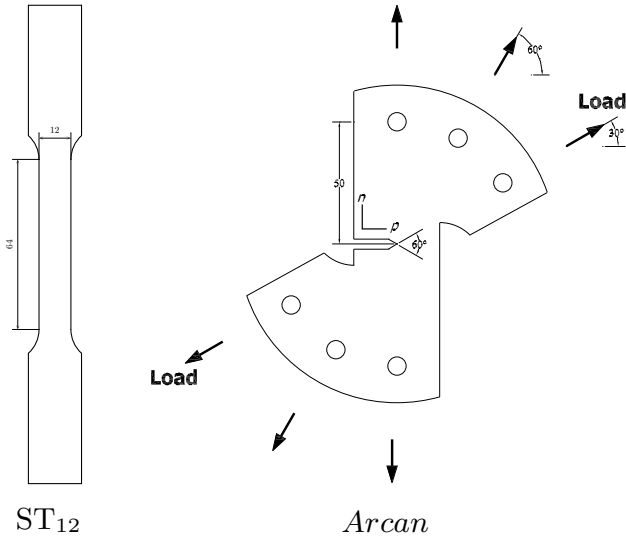
ST$_{12}$ Arcan
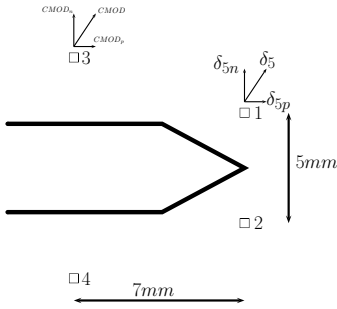
Figure 2: Specimens for mechanical testing.

Figure 3: Position of the series of marks used as optical extensometers in order to measure local displacement.

fracture zones. Between these voids, small dimples, probably initiated on dispersoids or Al$_2$(Cu,Mg) precipitates, are observed. The size of the triangular region depends on the loading angle (β) as shown in Fig. 4. It tends to decrease when mixity increases (i.e. low values for β).

5 Results of mechanical tests

5.1 Results for smooth specimens

Fig. 5 shows the nominal stress (F/S_0) as a function of axial longitudinal elongation (ϵ_L) and long transverse elongation (ϵ_T). It is shown that the material presents a plastic yielding anisotropy with the L direction being the strongest. These results are consistent with thus obtained by Bron for the similar 2024 Al Alloy plate although slight differences were found: higher hardening in the L–direction (higher
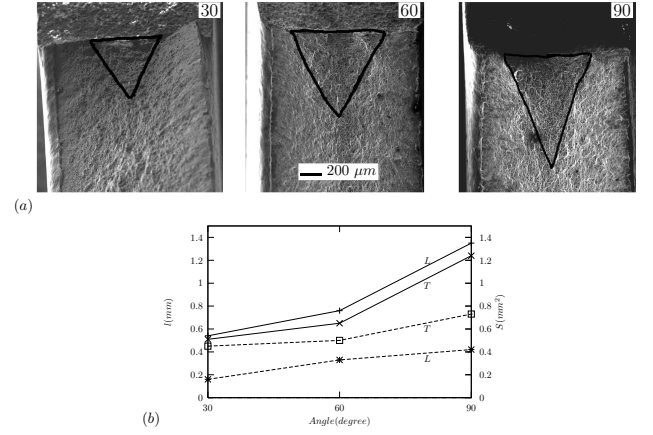

Figure 4: Fractographic examination: (a) Fracture surface SEM observations of Arcan sample (L$_N$ configuration), (b) Evolution of the triangular flat zone (length and surface) with respect to the loading angle β.

yield stress (YS) to ultimate stress (UTS) ratio) These data allow to compute the Lankford coefficient $\mathcal{L}_k$ defined as the ratio of the true deformation along the width of the specimen to the true deformation along the thickness (S direction). The latter is computed assuming plastic incompressibility. Results clearly indicate that thickness reduction is higher than width reduction. The principal mechanical characteristics are gathered in Table 2.

	YS (MPa)	UTS (MPa)	UE (%)	RE (%)	$\mathcal{L}_k$
L	394	468	15.	18.	0.69
T	332	455	15.	18.5	0.51–0.66

Table 2: Tensile properties along the L and T directions (YS: yield strength for 0.2% plastic strain (MPa), UTS: ultimate tensile strength (MPa), UE: uniform elongation (%), RE: elongation at rupture (%) deduced from the load line displacement corrected for elastic deformation, $\mathcal{L}_k$: Lankford coefficient for a plastic deformation of 5%.

5.2 Results for Arcan specimens

Results of Arcan tests are shown in Fig. 6. Both configurations L$_N$ and T$_N$ have very similar behavior showing that the ultimate force F_u and the corresponding displacement δ_{5u} increases when the mixity increases. The decomposition along normal and par-
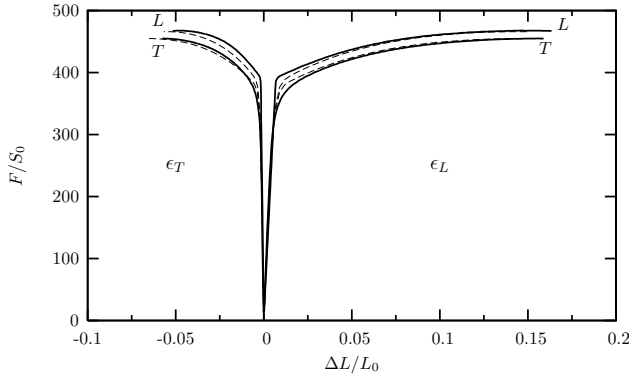
Figure 5: Tensile tests on ST_{12} along T and L directions: Nominal stress (F/S_0) as a function of axial engineering strain (ϵ_L) or long transverse engineering strain (ϵ_T). Dashed lines correspond to the FE simulation with the optimized coefficients presented on Table 4 and Table 5.

allel axes of the notch tip indicates, see Fig. 6 and Table 3, that the ultimate force F_u occurs approximately at a fixed value of the normal δ_5 displacement around $\delta_{5ni} = 0.24mm$ for L_N and $\delta_{5ni} = 0.25mm$ for T_N even though a slight decrease is observed for the loading condition $\beta = 30°$ (T_N configuration) corresponding to the mode II predominant mode. These observations were corroborated with the measurements of the $CMOD$ (not presented in the present paper). These results indicate the prevalence of Mode I fracture mechanisms dominated by tensile stresses. Similar results were obtained by [6] with the measurement of a crack-tip displacement vector δ_v except in pure Mode II, where a significant decrease of about 30% was observed. This last cases was not investigated in this study.

		F_u	F_{up}	F_{un}	δ_{5u}	δ_{5up}	δ_{5un}
	30°	6.72	5.82	3.35	0.43	0.37	0.22
L	60°	5.67	2.85	4.90	0.28	0.11	0.26
	90°	5.42		5.42	0.26		0.26
	30°	6.50	5.63	3.25	0.45	0.38	0.24
T	60°	5.66	2.84	4.90	0.26	0.11	0.24
	90°	5.25		5.25	0.24		0.24

Table 3: Decomposition of measured parameters along normal and tangential axes of the notch at the ultimate load, F: force (kN), δ_5: local extensometer (mm).
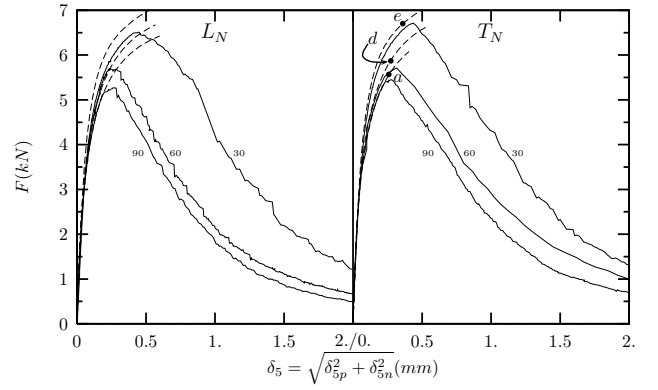

Figure 6: Arcan tests for T_N and L_N configurations: force—δ_5 curves for different samples. Dashed lines correspond to the FE simulation. Black dots indicate the predicted fracture initiation using Rice and Tracey indicator (dots marked as a, d and e corresponds to damage plots in Fig. 9).

6 Simulation — discussion

In this section, an interpretation of the main experimental results is proposed based on an application of the local approach to fracture [17]. Finite element simulation of various specimens was performed using the *Zset* software [18, 19]. Meshes were constructed using 3D elements with linear interpolation and full integration. Material symmetrie was used to reduce the problem size. Fig. 8 presents the 3D Arcan mesh used for FE simulation. An imposed displacement along the loading direction (β angle) is applied to the tip of two elastic wedges to represent pin loading without accounting for contact. In regions where damage develops, a fixed element size (about 50μm) was used.

6.1 Model for the plastic behavior

The material under study presents a complex anisotropic plastic behaviour which cannot be represented by a simple quadratic yield surface such as the one proposed in [20] which is unable to satisfactorily describe simultaneously yield anisotropy and Lankford coefficients in all directions. To overcome this difficulty, the yield condition proposed by [10] is used in this work. This phenomenological yield function is proposed to represent plastic anisotropy of aluminum alloy sheets. It is an extension of the functions given in [21] and [22]. Plastic anisotropy is represented by 12 parameters in the form of two fourth order symmetric tensors. Four other parameters influence the shape of the yield surface uniformly. The model is based on the definition of an equivalent stress $\overline{\sigma}$ function of the
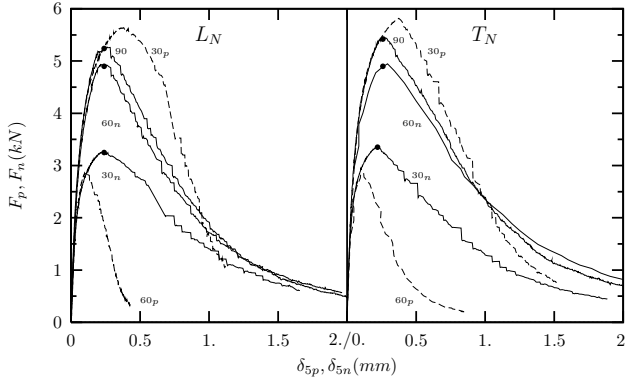
Figure 7: Arcan tests for T_N and L_N configurations: force—δ_5 curves projected along normal and parallel axes for different samples. Black dots indicate the positions of the ultimate Force F_u, Local displacement δ_{5n} for each case as reported on Table 3.

stress tensor $\underline{\sigma}$:

$$\overline{\sigma} = (\alpha_1 \overline{\sigma}_1^a + \alpha_2 \overline{\sigma}_2^a)^{1/a} \qquad (1)$$

with $\alpha_2 = 1 - \alpha_1$. $\overline{\sigma}_1$ and $\overline{\sigma}_2$ are respectively given by:

$$\overline{\sigma}_1 = \left(\frac{1}{2}\left(|S_1^2 - S_1^3|^{b_1} + |S_1^3 - S_1^1|^{b_1} + |S_1^1 - S_1^2|^{b_1}\right)\right)^{1/b_1} \qquad (2)$$

$$\overline{\sigma}_2 = \left(\frac{3^{b_2}}{2^{b_2}+2}\left(|S_2^1|^{b_2} + |S_2^2|^{b_2} + |S_2^3|^{b_2}\right)\right)^{1/b_2} \qquad (3)$$

where S_1^1, S_1^2 and S_1^3 (resp. S_2^1, S_2^2 and S_2^3) are the eigenvalues of a modified stress deviator $\underline{s}_1$ (resp. $\underline{s}_2$) defined as: $\underline{s}_1 = \underline{\underline{L}}_1 : \underline{\sigma}$ (resp. $\underline{s}_2 = \underline{\underline{L}}_2 : \underline{\sigma}$) where the fourth order tensors $\underline{\underline{L}}_{1,2}$ have the following form using Voigt notation:

$$\underline{\underline{L}}_k = \begin{pmatrix} (c_k^{LL}+c_k^{SS})/3 & -c_k^{SS}/3 & -c_k^{LL}/3 & 0 & 0 & 0 \\ -c_k^{SS}/3 & (c_k^{SS}+c_k^{TT})/3 & -c_k^{TT}/3 & 0 & 0 & 0 \\ -c_k^{LL}/3 & -c_k^{TT}/3 & (c_k^{TT}+c_k^{LL})/3 & 0 & 0 & 0 \\ 0 & 0 & 0 & c_k^{TL} & 0 & 0 \\ 0 & 0 & 0 & 0 & c_k^{LS} & 0 \\ 0 & 0 & 0 & 0 & 0 & c_k^{ST} \end{pmatrix} \qquad (4)$$

The yield surface is finally expressed as:

$$\Phi = \overline{\sigma} - R(p) \qquad (5)$$

where $R(p)$ represents isotropic work hardening parametrized by the effective plastic strain p. R is expressed as: $R(p) = R_0(1 + K_1(1 - \exp(-k_1 p)) + K_2(1 - \exp(-k_2 p)))$.

The identification of the various material parameters was performed following the procedure defined in [10]. Parameters representing plastic anisotropy are chosen as thus optimized by [10], see Table 5. Parameters representing elastic behavior and work hardening were identified using smooth specimens in L and T directions. The results are presented in Table 4 and Fig. 5 shows the comparison with tensile tests.

E	ν	R_0	K_1	k_1	K_2	k_2
69	0.36	277	0.35	664	0.71	10.54

Table 4: Parameters describing elasticity and plastic hardening. E: Young's modulus (GPa), ν: Poisson's ratio, R_0 (MPa).

$a = b_1 = b_2$	α	c_1^{TT} c_2^{TT}	c_1^{LL} c_2^{LL}	c_1^{SS} c_2^{SS}	c_1^{TL} c_2^{TL}
18.2	0.734	1.011	1.023	0.941	0.950
		0.797	0.646	1.276	1.188

c_i^{LS} and c_i^{ST}: these parameters are fixed to 1.

Table 5: Parameters describing anisotropic yielding and plastic flow, [10].

6.2 Evaluation of damage on Arcan specimens

The various tests carried out on Arcan specimens are simulated using the above described model. Good agreement is obtained up to the point for ductile failure initiation as shown in Fig. 6 which approximately corresponds to the load maximum.

Damage in the various specimens was evaluated based on a post–processing treatment of elasto-plastic calculations using the Rice and Tracey model for ductile void growth [23, 17]. The original model is however only valid for high stress triaxialities [24]. The accuracy of the model was improved by Huang [25] in particular to better represent void dilatation rate at low stress triaxiality. In that case the void growth rate is given by

$$\frac{\dot{R}}{R} = \begin{cases} \alpha \exp(\beta\tau)\dot{p} & \text{if } \tau > 1 \\ \alpha\tau^{1/4}\exp(\beta\tau)\dot{p} & \text{if } \tau \leq 1 \end{cases} \qquad (6)$$

where R is the void radius, τ the stress triaxiality, p the effective plastic strain. α and β are two constants which are equal to 0.427 and 1.5 respectively. Failure of a volume element is assumed to occur when void growth reaches a critical value $(R/R_0)_c$ (where R_0 is the initial void radius) which is assumed to be a material constant. A damage indicator (R/R_0) is obtained
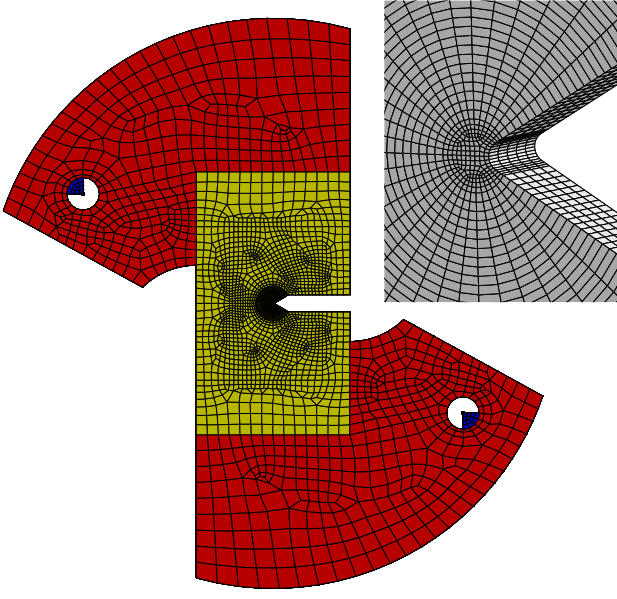
Figure 8: 3D Arcan mesh ($\beta = 30°$) used for FE simulation.

by integrating Eq. 6. The Rice and Tracey damage indicator was evaluated using averaged values of the plastic strain and the stress triaxiality ratio in each element. Numerical crack initiation is defined as the instant where the Rice and Tracey criterion is met for the first time in the structure. The crack extension at initiation corresponds to one element as averaged values are used.

In Fig. 9 the maximum value of damage are shown as a function of to δ_5 local displacement for both test configurations (L_N and T_N). For a given local displacement δ_5, one notices that damage increases when mixity is reduced. Maps (a), (b) and (c) show the damage indicator around the notch tip corresponding respectively to load angle β of $90°$, $60°$ and $30°$ for ($\delta_5 = \delta_{5u}$) at which the maximum load occurs for the case of Mode I (load angle of $90°$). It is clearly apparent that the introduction of external shear loading modifies the local state of damage. One notices that the orientation of damage contours is rotated counterclockwise (i.e towards the blunted portion of the notch surface) as β changes from $90°$ to $30°$. The damage indicator near the sharpened portion of the notch is small for the case involving a large Mode II component.

For $\beta = 90°$ (T_N configuration) the value of $(R/R_0)_c$ can be adjusted to represent failure initiation at the point $(\delta_5)_u = 0.26$ mm. $(R/R_0)_c = 1.82$ is then given by black dot (a) on Fig. 9. Using this value predicted failure initiation is represented by the black dots on Fig. 6 for the other load angles $\beta = 60°$

and $\beta = 30°$. For $\beta = 60°$ the initiation is well predicted whereas for $\beta = 30°$ initiation occurs slightly before the maximum load. The damage map (e) corresponding to this last case reveals a very different damage zone: the size of this zone is decreased compared to $\beta = 60°$ and $\beta = 90°$ cases.

When the load is closed to Mode I, the shape of damage zone is large and elongated from the notch tip as observed for plane stress condition. For the load close to Mode II ($\beta = 30°$), the shape of the damaged zones forms an asymmetric butterfly like shape as observed for plane strain conditions. These results are consistent with the size of the triangular region observed.

Finally, Fig. 10 shows the experimental curves are well reproduced by simulation. The critical values observed experimentally (black dots) indicate that the normal component of δ_5 at initiation (ultimate force) remains approximately constant whereas the parallel component varies greatly. Scatter has not been studied, this could explain the difference observed for the loading condition $\beta = 30°$ (T_N configuration).
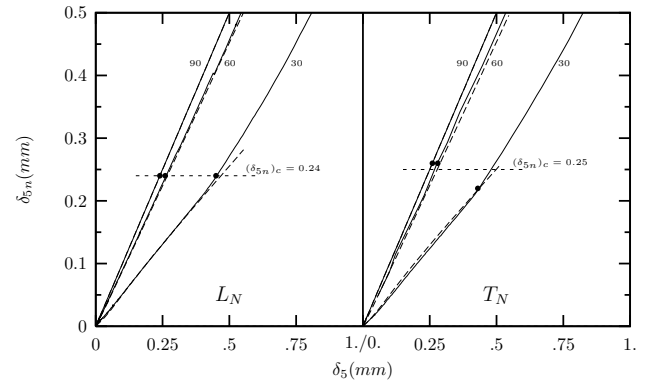

Figure 10: Arcan tests for T_N and L_N configurations: δ_5—δ_{5n} curves. Dashed lines correspond to the FE simulation. Black dots represent experimental failure initiation (corresponding to ultimate force F_u) for each case.

7 Conclusions

In this study, ductile rupture of a 2024 Al Alloy thin sheet was investigated under mixed-mode (I+II) loading. Mechanical tests were performed on smooth and specific mixed-mode Arcan specimens. Test data on smooth samples were used to identify the parameters of constitutive equations describing plastic anisotropy. Fracture initiation is studied using fractographic examination of broken specimens, measurements of local displacement fields in the vicinity of the V-notch
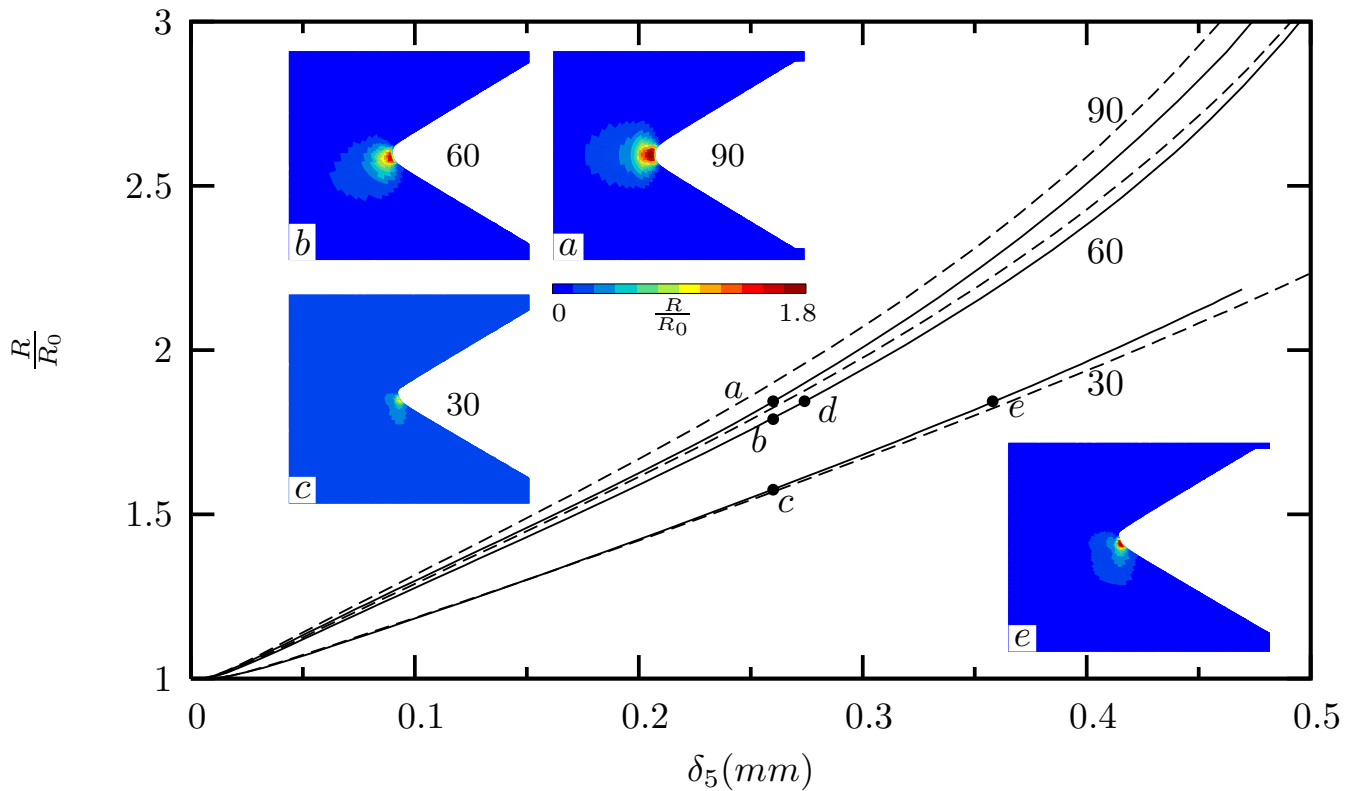
Figure 9: Arcan FE simulation: Rice and Tracey damage indicator (R/R_0) vs. δ_5 curves for different loading angles. Solid lines correspond to the L_N configuration while dashed lines correspond to T_N configuration. Maps show the damage indicator at various loading steps.

using Digital Image Correlation and finite element simulations of the whole Arcan specimen.

Fracture initiation is assumed to correspond to the load maximum and to the formation of the triangular area ahead of the initial notch. In this area damage is essentially controlled by void nucleation and growth. The corresponding δ_5 displacement increases when mixity is increased. It is however shown that its normal component δ_{5n} is constant. This conclusions are well supported by finite element simulations. Simulations also indicate that the size of the damaged zone at crack initiation decreases with increasing mixity which can be correlated with the decrease of the triangular area experimentally evidenced in Fig. 4. These results indicate that mode I component of loading mainly controls crack initiation. To validate these preliminary conclusions, further work will be carried out on fatigue precracked Arcan specimens. Lower loading angles β will also be used to further increase mode II loading. Note that under these conditions Arcan specimens tend to buckle. Finally full strain fields determined by DIC will be compared with FE simulations.

References:

[1] Qian, J. and Fatemi, A. (1996) *Eng. Fract. Mech.*, **55** (6), 969–990.

[2] Gao, X. and Shih, C. (1998) *Eng. Fract. Mech.*, **60** (4), 407–420.

[3] Besson, J., Madi, Y., Motarjemi, A., Koçak, M., Martin, G. and Hornet, P. (2005) *Mater. Sci. Engng A*, **397** (1–25), 84–91.

[4] Mahgoub, E., Deng, X. and Sutton, M. (2003) *Eng. Fract. Mech.*, **70**, 2527–2542.

[5] Zhang, X., Ma, S., Recho, N. and Li, J. (2006) *Eng. Fract. Mech.*, **73** (13), 1925–1939.

[6] Pirondi, A. and Dalle Donne, C. (2001) *Eng. Fract. Mech.*, **68** (12), 1385–1402.

[7] Simth, D., Swankie, T., Pavier, M. and Smith, M. (2008) *Eng. Fract. Mech.*, **75** (15), 4394–4409.

[8] (2004) *Local approach to fracture*. Presses de l'Ecole des Mines (Paris).

[9] Pineau, A. (2006) *Int. J. Frac.*, **138** (1-4), 139–166.

[10] Bron, F. and Besson, J. (2004) *Int. J. Plasticity*, **20**, 937–963.

[11] Bron, F., Besson, J. and Pineau, A. (2004) *Mater. Sci. Engng A*, **380**, 356–364.

[12] Bron, F. and Besson, J. (2006) *Eng. Fract. Mech.*, **73**, 1531–1552.

[13] Schwalbe, K.-H., Newman, J. and Shannon, J. (2005) *Eng. Fract. Mech.*, **72**, 557–576.

[14] Sutton, M., Yan, J., Cheng, C. and Zavattieri, P. (2007) *Optical Engineering*, **46**.

[15] Haddadi, H. and Belhabib, S. (2008) *Opt. Lasers Eng.*, **46** (2), 185–196.

[16] Sutton, M., Yan, J., Tiwari, V., Schreier, H. and Orteu, J. (2008) *Opt. Lasers Eng.*, **46** (10), 746–757.

[17] Pineau, A. (1992). In: *Topics in Fracture and Fatigue*, Argon, A. (Ed.), pp. 197–234. Springer Verlag Inc., NY.

[18] Besson, J. and Foerch, R. (1997) *Comp. Meth. Appl. Mech. Engng*, **142**, 165–187.

[19] Foerch, R., Besson, J., Cailletaud, G. and Pilvin, P. (1997) *Comp. Meth. Appl. Mech. Engng*, **141**, 355–372.

[20] (1950) *The mathematical theory of plasticity*. Clarendon Press, Oxford.

[21] Barlat, F., Lege, D. and Brem, J. (1991) *Int. J. Plasticity*, **7**, 693–712.

[22] Karafillis, A. and Boyce, M. (1993) *J. Mech. Phys. Solids*, **41**, 1859–1886.

[23] Rice, J. and Tracey, D. (1969) *J. Mech. Phys. Solids*, **17**, 201–217.

[24] Yatomi, M., Bettinson, A., O'Dowd, N. and Nikbin, K. (2004) *Fatigue and Fract. Engng Mater. Struct.*, **27** (4), 283–295.

[25] Huang, Y. (1991) *J. Applied Mech.*, **58**, 1084–1086.